Mimicking surface polaritons for unpolarized light with high-permittivity materials

Georgia T. Papadakis,[1,*] Artur Davoyan,[1,†] Pochi Yeh,[2] and Harry A. Atwater[1]
[1]*Thomas J. Watson Laboratories of Applied Physics, California Institute of Technology, California 91125, USA*
[2]*Department of Photonics, National Chiao Tung University, Hsinchu 30010, Taiwan*

(Received 13 July 2018; revised manuscript received 9 October 2018; published 10 January 2019)

Tailoring near-field optical phenomena often requires excitation of surface plasmon polaritons (SPPs) or surface phonon polaritons (SPhPs), surface waves at the interface between media with electric permittivities of opposite sign. Despite their unprecedented field confinement, surface polaritons are limited by polarization: only transverse magnetic fields enable their excitation, leaving transverse electric fields unexploited. By contrast, guided modes in positive permittivity materials occur for both linear polarizations, however, they typically cannot compete with SPPs and SPhPs in terms of confinement. Here we show that omnipolarization guided modes in materials with high-permittivity resonances can reach confinement factors similar to SPPs and SPhPs, while surpassing them in terms of propagation distance. We explore the cases of silicon carbide and transition-metal dichalcogenides near their permittivity resonances, and compare with SPhPs in silicon carbide and SPPs in silver, at infrared and visible frequencies, respectively.

DOI: 10.1103/PhysRevMaterials.3.015202

I. INTRODUCTION

Electromagnetic surface waves and their interaction with matter provide a path for tailoring near-field optical phenomena. The rise of plasmonics has generated excitement in a broad range of applications, for example, in medical technology [1], chemistry [2], lasers [3–5], optical circuitry [6–8], luminescence [9,10], and thermal management [11,12]. Surface plasmons are evanescent electromagnetic waves that propagate on a metallic surface [13] and exponentially decay in the lateral direction, as shown in Fig. 1(a). Their properties originate from the dispersion characteristics of Drude metals [black curve in Fig. 1(b)], and their uniqueness lies in their large mode confinement. In particular, the frequency dispersion of a surface plasmon polariton (SPP) exhibits a characteristic asymptotically increasing in-plane wavenumber k_{SPP}, which is unbound in the lossless limit [see Eq. (1) for $\epsilon(\omega) = -\epsilon_1$]. Therefore, the wavelength of a SPP ($\lambda_{\mathrm{SPP}} = 2\pi/k_{\mathrm{SPP}}$) can be up to ten times reduced compared to free-space wavelengths for noble metals [16], while this confinement factor can reach hundreds in graphene [17]. The asymptotic behavior of the SPP dispersion curve also yields a large density of optical states, a property desirable for engineering strong light-matter interactions with applications in luminescence, emission, and thermal control [11,18]. The prerequisite for excitation of SPPs is an interface between media with electric permittivities (ϵ) of opposite sign [19].

Aside from plasmonic metals with a broadband $\epsilon < 0$ below their plasma frequency, negative electric permittivity is also found at the Reststrahlen band of polar dielectrics [red curve in Fig. 1(b)]. In particular, the permittivity of polar dielectric materials exhibits Lorentz-shaped resonances at mid- to far-infrared (IR) frequencies, as a consequence of lattice vibrations, cf. phonons, in their crystal structure. The Reststrahlen band's $\epsilon < 0$ allows for excitation of surface phonon polaritons (SPhPs), which, similar to SPPs, are evanescent waves. In contrast to SPPs that originate from free charge carriers in metals, SPhPs occur due to bound charge oscillations in dielectrics [14,20,21].

Despite the unique electromagnetic features of SPPs and SPhPs, their excitation requires an out-of-plane electric field, which renders them relevant only for transverse magnetic (TM) fields, while they do not couple to transverse electric (TE) fields. Nevertheless, unpolarized light contains equal contributions of TE and TM components, therefore, the polarization dependence of surface (plasmon or phonon) polaritons constrains their relevance and limits the potential of plasmonic-based future technologies. To fully exploit the remarkable properties of SPPs and SPhPs as mechanisms for manipulating light in the nanoscale, for example, in harnessing solar energy [22,23], recycling heat [11,12,14], and controlling emission [3,9,10], it is valuable to explore means for overcoming this polarization bottleneck.

Here, we aim to alleviate the polarization dependence of SPPs and SPhPs by searching for material requirements for simultaneously accommodating TM and TE polarized surface waves. A naturally occurring TE equivalent to a surface polariton requires a material with $\mu < 0$, however, natural magnetism typically vanishes at IR and visible frequencies [19,24–27]. By contrast, guided modes in slabs of materials that exhibit a positive electric permittivity [see Fig. 1(c)] occur for both linear polarizations and have played a prominent role in integrated optical devices in the past decades [28,29]. Such guiding schemes can be very small by considering thin dielectric films of high-refractive index for compact optical circuitry [30–32]. The effective wavelength, or

*Present address: Department of Electrical Engineering, Ginzton Laboratory, Stanford University, California 94305, USA; gpapadak@stanford.edu
†Present address: Department of Mechanical and Aerospace Engineering, University of California, Los Angeles, California 90024, USA.

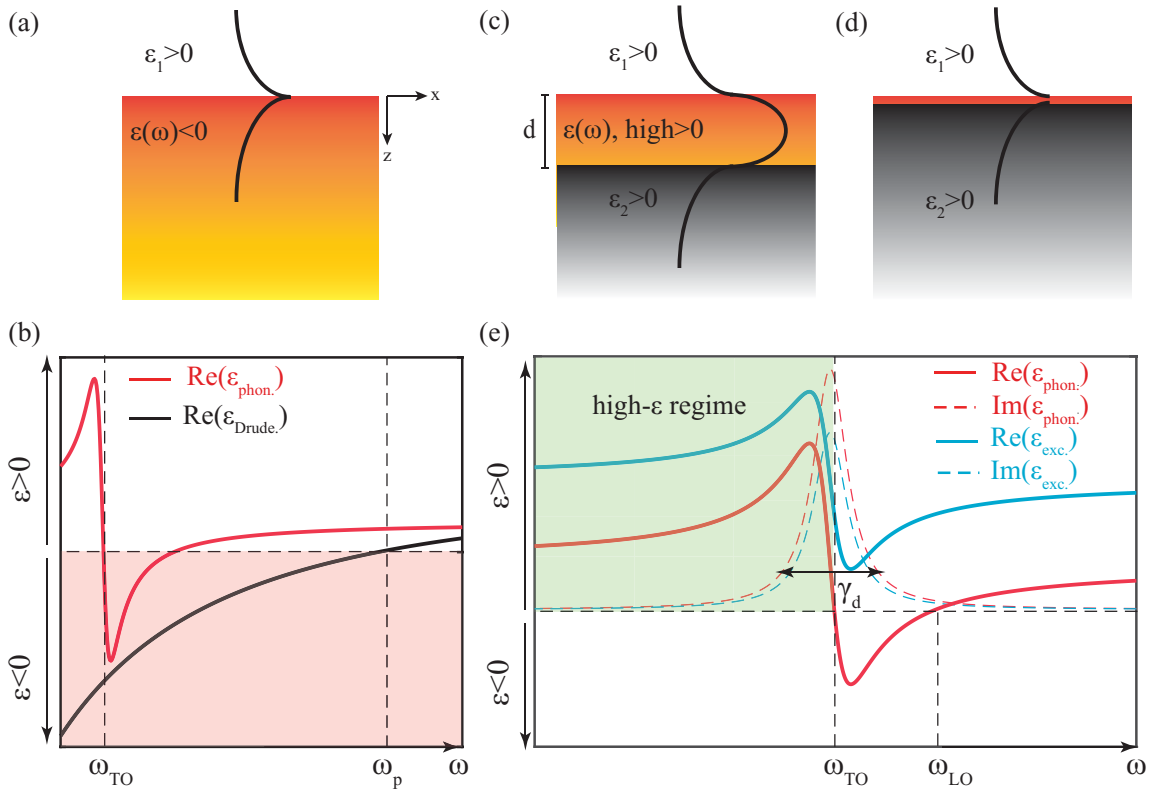

FIG. 1. Guided waves in $\epsilon < 0$ and $\epsilon > 0$ material systems. (a) At the interface between media with electric permittivities of opposite sign, surface plasmon polaritons (SPPs) and surface phonon polaritons (SPhPs) are supported. (b) Drude (black) and Lorentz (red) dielectric response, supporting SPPs and SPhPs, respectively, when $\epsilon < 0$ (red shaded region). (c) Guided waves are supported in slabs with high-ϵ, when embedded between lower-ϵ media. (d) Monolayer case of (c). (e) Electric permittivity of a polar dielectric material (red), where ω_{TO} and ω_{LO} correspond to the transverse and longitudinal optical phonon energies, respectively [14] [see Eq. (2)], and electric permittivity of an excitonic material (cyan), for example, transition-metal dichalcogenides (TMDs) [15]. For omnipolarization surface-confined propagation, we focus on the high-ϵ regime (green shaded region). Solid lines, real parts; dashed lines, imaginary parts. γ_d stands for the phonon and exciton lifetimes [see Eq. (2)].

confinement, of a guided mode scales with the refractive index as $\lambda_{eff} \sim \lambda_o/n$, where $n = \sqrt{\epsilon}$ and λ_o is the free-space wavelength. Hence, a large positive electric permittivity is key for exciting guided modes with strong interface confinement, for *both* linear polarizations, contrary to SPPs and SPhPs.

Such high-permittivity regimes are found, for example, on the red side of the Reststrahlen band of polar dielectric media, near their phonon resonances, in the IR range [see red curve in Fig. 1(e)]. Furthermore, large and positive permittivity resonances occur near the exciton transition energies of semiconductors [33] that lie at visible frequencies and typically exhibit Lorentz-shaped frequency dispersion, as shown with the cyan curve in Fig. 1(e). A set of polar dielectric materials and semiconductors with high-permittivity resonances is shown in Fig. 2, where the displayed wavelengths refer to the peak of their electric permittivity [frequency ω_{TO} in Fig. 1(e)]. An emerging class of semiconductors with particular interest to our study are transition-metal dichalcogenides (TMDs), namely, WS_2, MoS_2, WSe_2, and $MoSe_2$, that exhibit prominent features in their electric permittivity, both in their bulk and monolayer form, as recently discussed in [15].

In this work, we demonstrate that materials with pronounced permittivity resonances [green shaded regime in Fig. 1(e)] support omnipolarization guided modes [Figs. 1(c) and 1(d)] that can mimic the propagation characteristics of SPPs and SPhPs. As an example system in the IR range we investigate a slab of SiC, a polar dielectric material previously widely explored for SPhP propagation at its Reststrahlen band [11,14,20,21,34,35]. In contrast, here we focus on the high permittivity regime of SiC and compare with the SPhP band. At visible frequencies, we investigate TMDs near their excitonic resonances [15] and compare with SPPs on silver, since Ag is a state-of-the-art material for visible light plasmonics. For the selected materials, we show that omnipolarization surface-confined propagation is possible, with confinement similar to surface polaritons, and with propagation distance that surpasses them. We extend our findings to the monolayer case of TMDs [see Fig. 1(d)], where the high-ϵ modes have been previously termed exciton polaritons [36,37]. We start by demonstrating that the key material property enabling this response is a sharp and low-loss permittivity resonance, which we refer to as a high-quality factor (Q) in what follows.

II. HOW GUIDED MODES CAN COMPETE WITH SURFACE POLARITONS

At the interface between two media with electric permittivities $\epsilon_1 > 0$ and $\epsilon(\omega) < 0$, a TM-polarized surface excitation

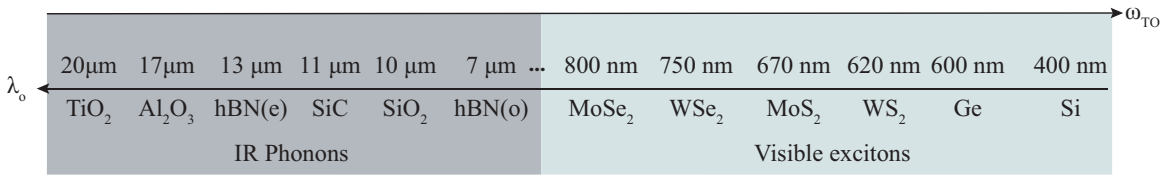

FIG. 2. Materials with Lorentz-type permittivity resonances at visible and IR frequencies. Polar dielectric materials at IR frequencies and excitonic materials (semiconductors) at visible frequencies exhibit high-ϵ Lorentz-type permittivity resonances (details for the selected materials can be found, for example, in [11,14,15]). ω_{TO} stands for the central frequency of the resonance [see Fig. 1(e)], near which surface-confined modes are computed in Figs. 4–6.

exists [Fig. 1(a)]. The frequency dispersion of its in-plane wavenumber is [13]

$$k_{\mathrm{SPP/SPhP}} = \sqrt{\frac{\epsilon(\omega)\epsilon_1}{\epsilon(\omega)+\epsilon_1}}k_{\mathrm{o}}, \tag{1}$$

where $k_{\mathrm{o}} = \omega/c$ is the free-space wavenumber. As $\epsilon(\omega)$ approaches $-\epsilon_1$, $k_{\mathrm{SPP/SPhP}}$ diverges, enabling extreme mode confinement. For metals, $\epsilon(\omega)$ is taken as the Drude model, $\epsilon(\omega) = 1 - \frac{\omega_{\mathrm{p}}^2}{\omega^2 + i\omega\gamma_m}$, where ω_{p} is the plasma frequency and γ_{m} is the inverse momentum-relaxation time of electrons. The SPP dispersion is shown with the black curve in Fig. 3 for a finite amount of loss γ_{m}. A similar dispersion characterizes SPhPs at the Reststrahlen band of polar dielectric materials

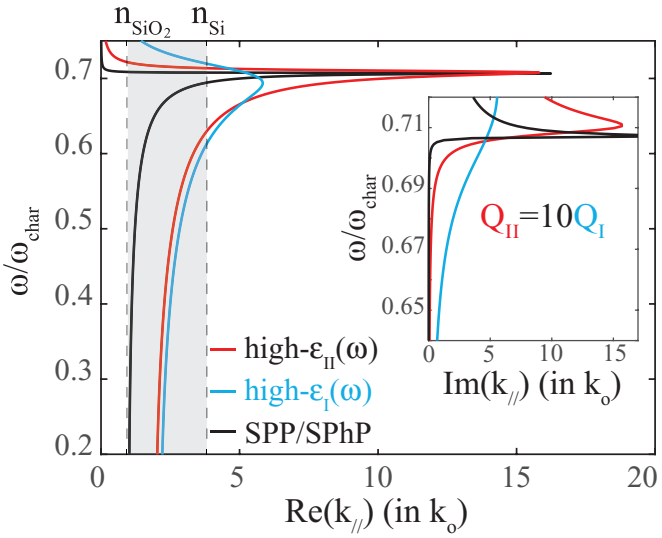

FIG. 3. SPPs and SPhPs compared to high-ϵ guided modes. The black curve denotes dispersion for SPPs [$\epsilon(\omega) < 0$, $\epsilon_1 = 1$; see Fig. 1(a) and Eq. (1)], for TM polarization. In this case, $\omega_{\mathrm{char}} = \omega_{\mathrm{p}}/\sqrt{2}$, where ω_{p} is the plasma frequency of Ag [38] and we take $\gamma_{\mathrm{m}} = 0.1\gamma_{\mathrm{m,Ag}}$. A similar dispersion characterizes SPhPs at IR frequencies. The grey shaded region denotes the dispersion regime of Si photonics: wavenumber values pertain to a typical Si waveguide on a SiO_2 substrate [$\epsilon_1 = 1$, $\epsilon(\omega) = \epsilon_{\mathrm{Si}}$, $\epsilon_3 = \epsilon_{\mathrm{SiO_2}}$; see Fig. 1(c)]. Cyan and red curves denote dispersion for guided modes in high-ϵ slabs [Fig. 1(c)], with $\epsilon_{1,3} = 1$, $\epsilon(\omega) = \epsilon_{\mathrm{Lor}}$ [Eq. (2)], for low and high-Q [Eq. (4)], respectively. We take $\omega_{\mathrm{char}} = \omega_{\mathrm{TO,I}} = \omega_{\mathrm{TO,II}}$ and $\gamma_{\mathrm{II}} = 0.1\gamma_{\mathrm{I}} = 7.267 \times 10^{13}$ rad/s [Eq. (2)], which is within the range of γ_{d} for most polar dielectric materials [11,14,21]. Inset: imaginary part of the in-plane wavenumber $k_{//}$.

that can be described with the Lorentz model

$$\epsilon_{\mathrm{Lor}}(\omega) = \epsilon_{\infty,\mathrm{d}}\left(\frac{\omega_{\mathrm{LO}}^2 - \omega^2 - i\gamma_{\mathrm{d}}\omega}{\omega_{\mathrm{TO}}^2 - \omega^2 - i\omega\gamma_{\mathrm{d}}}\right), \tag{2}$$

where ω_{LO} and ω_{TO} correspond to the longitudinal and transverse phonon energies, respectively, and γ_{d} is the inverse phonon lifetime. The back-bending of the SPP/SPhP dispersion curve in Fig. 3 arises from material loss, in other words, from the nonzero values of γ_{m} or γ_{d} in Drude metals and polar dielectric materials, respectively [13,16,39]. This back-bending determines the maximum wavenumber $k_{\mathrm{SPP/SPhP}}$ that corresponds to the highest degree of confinement and is bounded by material loss. A nonzero imaginary component of the wavenumber, $\mathrm{Im}(k_{\mathrm{SPP/SPhP}})$, also arises from material loss, and its frequency dispersion is shown with the black curve in the inset of Fig. 3.

Next, we consider a slab of thickness d of an arbitrary material with positive permittivity $\epsilon(\omega)$, sandwiched between two semi-infinite spaces with permittivities $\epsilon_{1,2}$ [Fig. 1(c)], where we set $\epsilon(\omega) > \epsilon_{1,2}$. By selecting appropriately the thickness d of the slab, one can engineer the TE guided modes to overlap in frequency (ω) and in-plane wavenumber ($k_{//}$) with the TM ones, thereby leading to omnipolarization, phase-matched propagation [see Figs. 4(a) and 5(a)–5(d)]. In this configuration, $k_{//}$ is bounded by the refractive indices of the surrounding and guiding media, and its maximum value is

$$k_{\mathrm{max}} = \max\{\sqrt{\epsilon(\omega)}\}k_{\mathrm{o}}. \tag{3}$$

For example, a widespread waveguide system in silicon photonics is a Si slab sandwiched between air and a SiO_2 substrate. At $\lambda_{\mathrm{o}} = 1.5$ μm, SiO_2 and Si exhibit negligible frequency dispersion, and their refractive indices are 1.5 and 3.4, respectively. Therefore, the in-plane wavenumber is bounded by $1.5 \leqslant k_{//}/k_{\mathrm{o}} \leqslant 3.4$. This regime is shown with the grey shaded area in Fig. 3. By considering that the effective wavelength of a guided mode is given by $\lambda_{\mathrm{eff}} = 2\pi/k_{//}$, it is easy to see that silicon photonic guided modes cannot typically compete with SPPs or SPhPs in terms of confinement.

Now let us consider a dispersive electric permittivity $\epsilon(\omega)$ for the slab [Fig. 1(c)], and particularly $\epsilon(\omega) = \epsilon_{\mathrm{Lor}}(\omega)$, and let us focus in the high-ϵ frequency range [green shaded area in Fig. 1(e)], for $\omega \lessapprox \omega_{\mathrm{TO}}$. We define the material quality factor Q, with respect to Eq. (2), as

$$Q = \frac{\omega_{\mathrm{TO}}}{\gamma_{\mathrm{d}}}. \tag{4}$$

The quality factor Q expresses the sharpness of the permittivity resonance [Fig. 1(e)]. In Fig. 3 we plot the maximum

wavenumber k_{max} [Eq. (3)] for two different values of Q (cyan and red curves). It can be seen that, by increasing Q, one obtains larger $\mathrm{Re}(k_{//})$, and hence improved confinement, while also achieving low propagation losses, since the parameter $\mathrm{Im}(k_{//})$ decreases considerably near resonance, for increasing Q. It is noteworthy that the dispersion curve for high-Q material slabs (red curve in Fig. 3) resembles the SPP/SPhP dispersion curve (black curve in Fig. 3). This highlights that guided modes in high-Q materials can reach surface confinement similar to SPPs and SPhPs. We note that for the SPP dispersion in Fig. 3 we selected $Q_{SPP} = \omega_p/\gamma_m = 1.88 \times 10^3$, which is an overestimation of the quality factor of most plasmonic metals (for reference, $Q_{Ag} = 1.88 \times 10^2$ [38]).

In Fig. 3 we demonstrated that, in principle, guided modes in high-ϵ material slabs can compete with surface polaritons in terms of confinement. By defining the propagation distance of a mode as $L = 1/2\mathrm{Im}(k_{//})$, we also see, from the inset of Fig. 3, that such modes can propagate for longer distances, compared to SPPs or SPhPs. We emphasize that both TE and TM guided modes are supported in high-ϵ material slabs, thereby alleviating the polarization limitation of surface polaritons. The key material parameter for highly confined guided modes is large Q. In contrast to the maximum value of $k_{SPP/SPhP}$, which is bounded by loss [Eq. (1)], the maximum wavenumber of a guided mode is bounded by $\max\{\epsilon(\omega)\} = \epsilon(\omega_{TO})$ [Eq. (3)]. As Q increases, permittivity resonances become sharper and $\epsilon(\omega_{TO})$ increases. This also leads to increased losses on resonance; however, this issue is overcome by operating slightly off resonance, to the red side of ω_{TO}.

In what follows we perform detailed surface wave calculations for selected high-Q materials and compare them with surface polaritons in terms of confinement, mode volume, and propagation distance. By modeling the electric permittivity for the selected materials with the Lorentz model [Eq. (2)], we derive a quality factor Q [Eq. (4)] for each one. In the search for high-permittivity materials with pronounced resonances, we resort to polar dielectrics and TMDs at IR and visible frequencies, respectively. In the IR range, we select SiC due to its very large $Q_{SiC} = 166$ [11] (we note that even higher values of Q_{SiC} have been reported [14,21,34,35]). The high-Q guided modes of SiC are compared to its SPhP in the Reststrahlen band (Fig. 4). At visible frequencies, we compare SPPs in silver with guided modes in thin films (Fig. 5) and monolayers (Fig. 6) of WS_2, MoS_2, WSe_2, and $MoSe_2$. These materials support prominent permittivity resonances that span the whole visible spectrum (see Fig. 2), as reported experimentally by Li *et al.* [15]. By fitting the data from [15] with Eq. (2) we obtain, for bulk properties, $Q_{WS_2} = 37$, $Q_{MoS_2} = 25$, $Q_{WSe_2} = 18$, and $Q_{MoSe_2} = 19$, while slightly higher quality factors describe monolayers.

In the dispersion curves that follow, in order to provide a direct estimation of confinement and to facilitate comparison between results pertaining to different frequency ranges, the in-plane wavenumber $k_{//}$ is normalized to k_o. Since $k_{//}/k_o = \lambda_o/\lambda_{eff}$, the horizontal axes of the dispersion curves that follow display the number of modal wavelengths that fit in the wavelength of excitation, λ_o. Furthermore, we define the effective propagation length as

$$L_{eff} \equiv \frac{\mathrm{Re}(k_{//})}{\mathrm{Im}(k_{//})} = 4\pi \frac{L}{\lambda_{eff}} \tag{5}$$

that expresses the number of modal wavelengths or cycles that a wave propagates prior to decaying. The normalization of the absolute propagation length L to λ_{eff} also facilitates comparison between results at different frequency ranges. Furthermore, we introduce the modal cross-section area [40], which, in the one-dimensional case studied here, is given by

$$A_{eff} \equiv \frac{A_{1D}}{A_{o,1D}} = \frac{[\int I dz]^2/\int I^2 dz}{\lambda_o/2}, \tag{6}$$

where I is the intensity profile of the mode [$E^2(z)$ or $B^2(z)$, where z is the out-of-plane direction; see Fig. 1(a)]. We normalize to $A_{o,1D} = \lambda_o/2$, which is the diffraction-limited spot in one dimension. The limits of integration in Eq. (6) are taken to be on the order of tens of wavelengths away from the area where the mode is confined.

The mode detection scheme used in the results that follow is the reflection pole method [41]. Although this work focuses on guided modes in single layers, our methodology applies to any multilayer configuration of finite thickness, in contrast to Bloch-based approaches for infinitely periodic superlattices [42]. By additionally employing a parameter retrieval [43], we introduce conditions for distinguishing between surface-confined and leaky modes. For details see Appendix A.

III. RESULTS

A. High-ϵ modes in SiC versus SPhPs

In the IR spectral range, polar dielectrics exhibit permittivity resonances due to lattice vibrations or phonons. An overview of the properties of a number of high-Q polar dielectrics can be found in [14]. We select SiC due to its very large quality factor $Q_{SiC} = 166$, which is a prerequisite for guided modes with large confinement, as discussed in Sec. II. The IR permittivity of SiC is most widely described with Eq. (2), using $\epsilon_{\infty,d} = 6.7$, $\omega_{TO} = 1.49 \times 10^{14}$ rad/s, $\omega_{LO} = 1.83 \times 10^{14}$ rad/s, and $\gamma_d = 8.97 \times 10^{11}$ rad/s [11,12,44].

We start from a semi-infinite slab, where TE and TM modes in the positive permittivity regime ($\omega \leqslant \omega_{TO}$) are degenerate. We gradually decrease the thickness of the slab d until reaching the minimum thickness for which the TE and TM dispersion curves of the guided modes remain degenerate. This occurs at $d = 8\pi c/(\omega_{TO}\sqrt{\epsilon_{SiC}(\omega_{TO})}) \simeq 3\ \mu$m. We consider Si as the substrate material and set its refractive index to $n_{Si} = 3.4$ [45,46].

As can be seen from Fig. 4(a), in the Reststrahlen band (red shaded area), there exists a TM-polarized SPhP, due to $\epsilon_{SiC} < 0$. The SPhP is highly localized at the air-SiC interface, as is shown with the field profile in the upper inset. Its effective cross-section area falls in the range $A_{eff,SPhP} \sim [0.03, 0.09]$, which is considerably smaller than the mode volume of SPhPs in the majority of polar dielectric materials [11,14,21]. From Fig. 4(b), it is also seen that the propagation length L_{eff} of the SPhP decreases for increasing frequency as one approaches the maximum value of $k_{SPhP} \sim 12k_o$ [Fig. 4(a)].

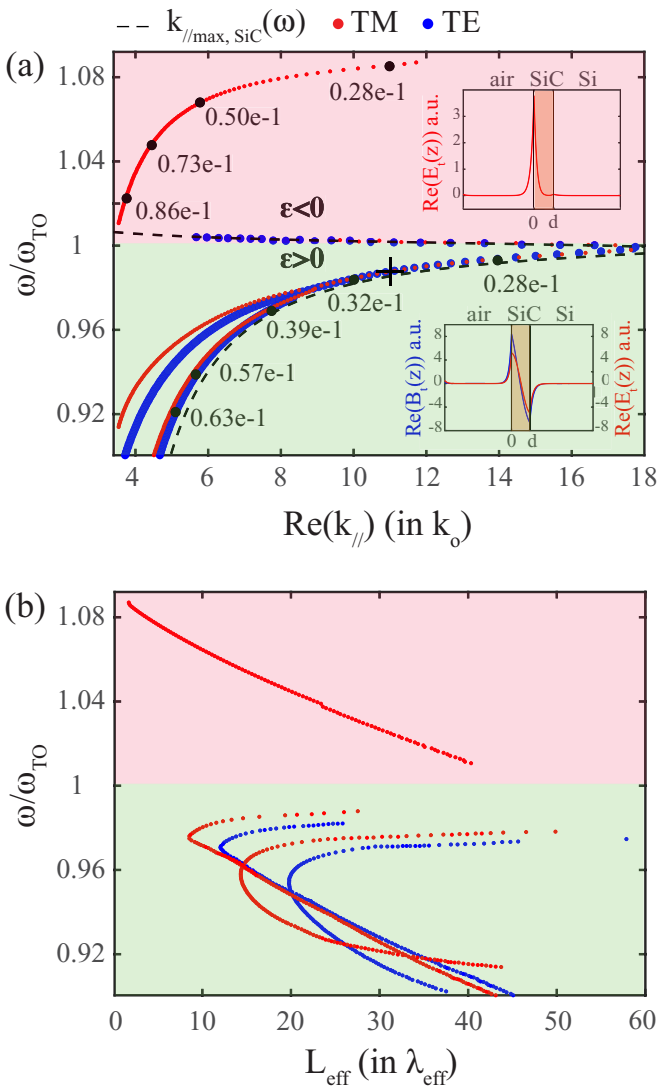

FIG. 4. Surface-confined modes in a thin film of SiC on Si as compared to SPhPs. (a) Dispersion curves and (b) propagation length [Eq. (5)] for surface-confined waves supported in a slab of SiC on Si, in the IR frequency regime. The green shaded area emphasizes the high-ϵ regime, where simultaneous excitation of TE (blue) and TM (red) surface-confined waves with overlapping dispersion curves occurs (crossing point indicated with the cross mark), with similar dispersion characteristics to the SiC SPhP, displayed in the red shaded regime. The SPhP occurs at frequencies $\omega > \omega_{\mathrm{TO}}$, for which $\epsilon_{\mathrm{SiC}} < 0$ (Reststrahlen band [14]). Numerical results presented as points in (a) correspond to values of the cross-section area of the mode [Eq. (6)]. The dashed line in (a) corresponds to $k_{\mathrm{max}} = \sqrt{\epsilon_{\mathrm{SiC}}(\omega)}k_{\mathrm{o}}$.

In contrast to the Reststrahlen band, where the SPhP is restricted to TM polarization, in the high-ϵ regime shown in the green shaded area in Fig. 4(a), simultaneously TE- and TM-polarized guided modes exist with overlapping dispersions. In Fig. 4 we display the guided modes that exhibit the largest $k_{//}$; however, we note that lower-order (lower-$k_{//}$) modes also occur but are not highly confined. We observe that the maximum in-plane wavenumber, or parameter k_{max} in Eq. (3), is very large, i.e., $k_{\mathrm{max}} \sim 18k_{\mathrm{o}}$, which follows from the large value of $\sqrt{\epsilon(\omega_{\mathrm{TO}})} \sim 20$ in SiC. Therefore, we see that, despite the fact that these guided modes cannot be strictly classified as surface waves, they resemble them due to their high degree of mode confinement. Furthermore, the effective cross-section area A_{eff} of the guided modes is comparable to the SiC SPhP for the same $k_{//}$, namely, $A_{\mathrm{eff}} \sim [0.03, 0.06]$, and their field profiles for both linear polarizations are shown in the lower inset of Fig. 4(a). These modes exhibit increasing propagation distance [green shaded area in Fig. 4(b)] as the frequency is tuned off resonance ($\omega < \omega_{\mathrm{TO}}$), which stems from the tradeoff between confinement and propagation distance.

Other polar dielectrics with high-permittivity resonances at IR frequencies can also support similar surface-confined omnipolarization guided modes that can compete with their respective SPhPs, for example, SiO_2 [35] and hBN [20,47] [see Fig. 2].

B. High-ϵ modes in TMDs versus SPPs in silver

In the visible part of the spectrum, excitonic resonances in semiconducting materials yield frequency regimes of large electric permittivity. For Si and Ge, for example, these resonances occur near $\lambda_{\mathrm{o}} = 400$ nm [45,46] and $\lambda_{\mathrm{o}} = 600$ nm [46], respectively. Nevertheless, for most semiconductors, the exciton lifetime [γ_{d}^{-1} in Eq. (2)] is rather small, leading to low-Q permittivity resonances that are not ideal for the concept of highly confined guided waves outlined in Sec. II.

By contrast, excitons in TMDs induce sharp permittivity features [15], therefore, TMDs can serve as material platforms for highly confined guided waves. Each TMD investigated here (WS_2, MoS_2, WSe_2, and $MoSe_2$) has a number of permittivity resonances at visible frequencies, originating from various electronic transition mechanisms. We focus on the frequency regime near the highest-Q permittivity resonance for each material. These span the whole visible spectral range and are located at $\omega_{\mathrm{TO}} = 2.37 \times 10^{15}$ rad/s ($\lambda_{\mathrm{o}} \simeq 795$ nm) for $MoSe_2$, $\omega_{\mathrm{TO}} = 2.5 \times 10^{15}$ rad/s ($\lambda_{\mathrm{o}} \simeq 753$ nm) for WSe_2, $\omega_{\mathrm{TO}} = 2.75 \times 10^{15}$ rad/s ($\lambda_{\mathrm{o}} \simeq 685$ nm) for MoS_2, and $\omega_{\mathrm{TO}} = 3 \times 10^{15}$ rad/s ($\lambda_{\mathrm{o}} \simeq 630$ nm) for WS_2. The quality factors associated with these resonances, as fitted via Eq. (2), are $Q_{\mathrm{MoSe_2}} = 19$, $Q_{\mathrm{WSe_2}} = 18$, $Q_{\mathrm{MoS_2}} = 25$, and $Q_{\mathrm{WS_2}} = 37$, respectively.

Similar to the case of SiC described above, we start by considering bulk degenerate modes for TE and TM polarizations, and gradually decrease the thickness of the TMD slab until we reach the smallest thickness for which the highest $k_{//}$ TE and TM guided modes remain degenerate in both frequency and wavenumber. This occurs approximately at $d = 6\pi c/(\omega_{\mathrm{TO}}\sqrt{\epsilon(\omega_{\mathrm{TO}})})$ for all considered TMDs, and the dispersion of these guided modes is shown in the upper panels of Figs. 5(a)–5(d). We display only the two largest $k_{//}$ guided modes for each polarization, similar to Sec. III A, however, we note that lower-order (smaller-$k_{//}$) and less-confined guided modes also occur but are outside the scope of this work. We consider SiO_2 as a substrate material, and set its refractive index to $n_{\mathrm{SiO_2}} = 1.5$. The field profiles of the larger-$k_{//}$ modes for both linear polarizations are shown with the inset in Fig. 5(d), lower panel, for WS_2, and similar field profiles correspond to modes in MoS_2 and WSe_2 and in $MoSe_2$. For the sake of comparison with a conventional plasmonic mode,

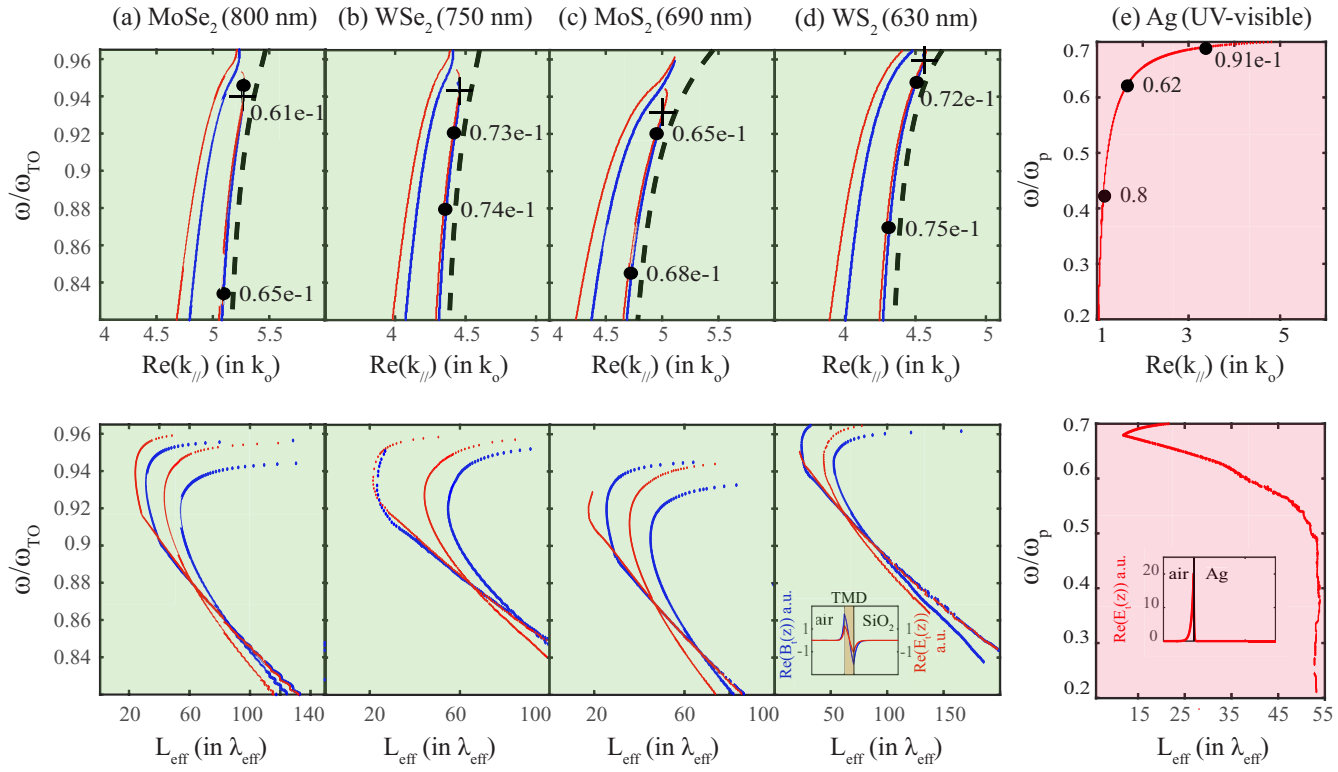

FIG. 5. Surface-confined modes in thin films of TMDs on SiO_2 as compared to SPPs on Ag. Dispersion curve (upper panels) and propagation length [Eq. (5)] (lower panels) for surface-confined waves supported on a slab of (a) $MoSe_2$, (b) WSe_2, (c) MoS_2, and (d) WS_2, compared to (e) SPPs on semi-infinite Ag. Red corresponds to TM polarization while blue corresponds to TE polarization. Numerical results presented as points in the upper panels correspond to values of the cross-section area of the mode [Eq. (6)]. Dashed lines in (a)–(d) (upper panels) correspond to $k_{max} = \sqrt{\epsilon(\omega)}k_o$. Crossing points of TE and TM dispersion curves are indicated with the cross marks in the upper panels.

we display in Fig. 5(e) the dispersion of a SPP mode at the interface between Ag and air. For Ag, we used the Drude model with $\omega_p = 13.69 \times 10^{15}$ rad/s and $\gamma_m = 0.7292 \times 10^{14}$ rad/s from [38]. The field profile of the SPP mode on Ag is shown with the inset in Fig. 5(e), lower panel.

By considering the confinement factor $k_{//}$ displayed on the horizontal axes in the upper panels of Figs. 5(a)–5(e), we infer that, in fact, guided modes in TMDs are more confined compared to the SPP mode on Ag in the visible spectral range [i.e., for $\omega/\omega_p < 0.34$ in Fig. 5(e)]. This stems from the large value of refractive index $\sqrt{\epsilon(\omega_{TO})}$ in TMDs, which yields large k_{max} [Eq. (3)]. It is noteworthy that the cross-section area A_{eff} [Eq. (6)] of these guided modes is an order of magnitude smaller than that of the SPP mode on Ag in the low-damping regime (for $\omega/\omega_p \ll 1$). As the frequency of the SPP mode approaches the surface plasmon frequency $\omega_{sp} = \omega_p/\sqrt{2}$, the SPP confinement increases, as seen with the value $A_{eff,SPP} = 0.091$ in Fig. 5(e); however, this frequency regime corresponds to ultraviolet light.

Furthermore, the propagation distance of the TMD guided modes [lower panels in Figs. 5(a)–5(d)] is greater than that of a SPP mode on Ag [lower panel in Fig. 5(e)], which is enabled by the large quality factors Q in TMDs that yield small material loss even for frequencies very close to ω_{TO} [Fig. 1(e)]. By contrast, the large and broadband losses of silver at optical frequencies lead to smaller L_{eff}, which nearly vanishes at ω_{sp}.

To conclude this section, we showed that large confinement factors typically found in SPP modes on Ag can also occur in guided modes in thin films of TMDs. These modes occur for both linear polarizations contrary to SPPs, and it is important to note that they can travel for larger propagation distances at visible frequencies.

C. High-ϵ modes in monolayer TMDs

In this section we assess the four TMDs discussed in the previous section as guiding materials in their monolayer form, as depicted in Fig. 1(d). Previous work in monolayer TMDs [48] has discussed the existence of these modes in MoS_2 and WSe_2 [36,49], and in WS_2 [37], however, most previous reports have focused on the exciton dynamics and not on the dispersion, confinement, and propagation distance of the guided modes [50,51] associated with these excitons. In Fig. 6 we carry out a systematic study of the dispersion and propagation distance for the monolayer guided modes associated with the most prominent permittivity resonances in WS_2, MoS_2, WSe_2, and $MoSe_2$, as reported in the experimental results by Li *et al.* [15].

The TMDs discussed here transition from indirect to direct band gap in their monolayer form, for which their quality factors slightly increase to $Q_{MoSe_2,mono} = 29$, $Q_{WSe_2,mono} = 32$, $Q_{MoS_2,mono} = 26$, and $Q_{WS_2,mono} = 77$, with respect to the values reported for bulk in Sec. III B. Similar to Sec. III B, we remain in the wavelength range of

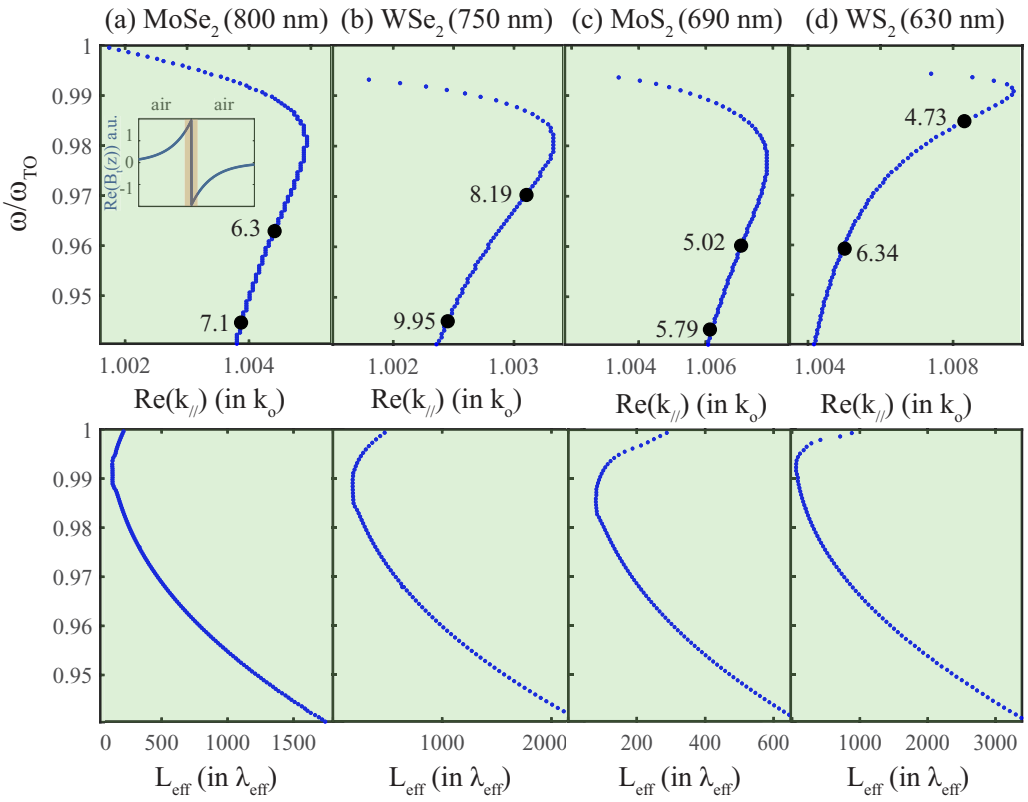

FIG. 6. Surface-confined modes in monolayer TMDs. Dispersion curve (upper panels) and propagation length [Eq. (5)] (lower panels) for TE-polarized surface-confined waves supported on a monolayer of (a) $MoSe_2$, (b) WSe_2, (c) MoS_2, and (d) WS_2. Numerical results presented as points (upper panels) correspond to values of the cross-section area of the mode [Eq. (6)].

$\lambda_o \simeq 795$ nm, $\lambda_o \simeq 753$ nm, $\lambda_o \simeq 685$ nm, and $\lambda_o \simeq 630$ nm, for $MoSe_2$, WSe_2, MoS_2, and WS_2, respectively.

In the monolayer case, the TM-polarized guided mode discussed previously (Fig. 5) experiences a cutoff, and only the TE polarization survives [36]. Figure 6 displays the dispersion relation near ω_{TO} (as given in Sec. III B). At ω_{TO} the TE guided mode reaches its maximum confinement ($k_{//}$), however, the near-zero thickness of the monolayers largely reduces the confinement factor compared to the TMD slabs of finite thickness evaluated in the previous section. As a consequence, the cross-section area increases, and the monolayer TMD modes are confined to roughly a couple of micrometers, which is in agreement with predictions in [36]. The decrease in confinement is, nevertheless, accompanied by a considerable increase in propagation distance. As seen in the lower panels in Figs. 6(a)–6(d), L_{eff} can be as large as hundreds to thousands of modal wavelengths, which follows from the indirect to direct band gap transition in the monolayer case or, in other words, from the increase in quality factor, Q, compared to bulk TMDs.

IV. CONCLUSIONS

In nanoscience, tailoring electromagnetic phenomena in the near-field is enabled via evanescent waves. The excitation of surface waves at the interface between different electromagnetic media requires opposite signs of electric permittivities or magnetic permeabilities for TM and TE polarization, respectively. However, the lack of magnetic materials at high frequencies leads to a natural asymmetry in surface wave propagation, which is only accessible for TM polarization. Here, we proposed a concept for circumventing this limitation with guided modes in slabs of materials with positive and large permittivity. Contrary to surface polaritons, these guided modes can occur for both linear polarizations simultaneously. We showed that the material requirement for omnipolarization surface wave propagation with high degree of surface confinement and large propagation distance is a large material quality factor. As example materials, we studied SiC at IR frequencies and TMDs at visible frequencies, and demonstrated that the omnipolarization guided modes in these systems can compete with SPhPs in SiC and SPPs in Ag at IR and visible frequencies, respectively, in terms of both confinement and propagation distance.

We note that the large in-plane wavenumber of highly confined modes and surface waves ($k_{//} > k_o$) renders them nonradiative, which introduces a phase mismatch with free-space radiative modes ($k_{//} < k_o$). Therefore, excitation and detection in the far-field requires a grating [16,52–55], scattering center, e.g., a slit [52], or a prism [30] or overlayer [26]. A prism or an overlayer achieves coupling to free-space by shifting the dispersion of photons to larger wavenumbers ($k_{prism} = n\omega/c > k_o$, where n is the refractive index of the prism or overlayer). A grating with periodicity Λ_g ascribes an additional wavenumber component to the scattered field, $k_g = 2\pi/\Lambda_g$, therefore, coupling to any wavenumber and corresponding frequency can be achieved by controlling Λ_g, as has been previously shown for SPPs [53–55]. The grating

configuration is particularly relevant to the modes proposed here, because the dispersion overlap in frequency and wavenumber between the two polarizations (Figs. 4–6) renders them phase matched, i.e., $k_{//\mathrm{TE}} = k_{//\mathrm{TM}}$. Therefore, a single grating may be used for excitation and detection of both polarizations at a single frequency. Alternative excitation schemes include injection of an electron beam [54], or coupling to a dipole moment in the near-field, for example, via scanning near-field optical microscopy [47–49].

Our results convey that the polarization bottleneck of plasmonics may be alleviated with high-Q positive permittivity polar dielectrics and semiconductors. These systems can support omnipolarization phase-matched surface-confined guided modes with large propagation distances.

ACKNOWLEDGMENTS

This work was supported by U.S. Department of Energy (DOE) Office of Science Grant No. DE-FG02-07ER46405 (G.T.P. and H.A.A.) and the Air Force Office of Scientific Research (A.R.D.) under Grant No. FA9550-16-1-0019. G.T.P. acknowledges support by the American Association of University Women Dissertation Fellowship and the TomKat Postdoctoral Fellowship in Sustainable Energy at Stanford University, and fruitful discussions with R. Pala.

APPENDIX A: SURFACE WAVES DETERMINATION VIA HOMOGENIZATION

The boundary condition problem of a guided or surface mode at a single interface may be analytically treated [13,39,56], however, larger systems such as single slabs and multilayers require a numerical solver [41,57–65]. Here, we present our methodology for computing the modes discussed in Figs. 4–6. Our approach is general and applies to any planar heterostructure of finite thickness, while also being able to distinguish between eigenmodes that constitute surface waves, i.e., modes that exponentially decay away from the interface of interest, and leaky modes, that oscillate in the out-of-plane (z) direction [see Fig. 7(b)].

A schematic of the general structure we investigate is displayed in Fig. 7(a). We consider a layered arrangement consisting of an arbitrary number of layers of nonmagnetic materials in an arbitrary sequence, with layer thicknesses that may be in the subwavelength limit ($d_i \ll \lambda_o$) or thicker. Using the transfer matrix formalism for layered media [66], we obtain the matrix $\bar{M}$ elements $m_{11}(k_{//}, \omega)$ and $m_{21}(k_{//}, \omega)$ for varying in-plane wavenumber $k_{//} = k_x$ and frequency ω. The transmission and reflection complex coefficients are then given by $t = 1/m_{11}$ and $r = m_{21}/m_{11}$, respectively. We seek surface waves and guided modes by first determining the full set of eigenmodes of the heterostructure, for which $t \to \infty$, $r \to \infty$ [66]. Alternatively, the eigenmodes are zeros of the matrix element $m_{11}(k_{//}, \omega)$. We employ the reflection pole method (RPM) [41], which is based on the residue theorem of complex analysis, for detecting these zeros in the complex plane. Zeros of the complex function m_{11} yield phase shifts of $\mathrm{Arg}(m_{11}) = \pi$ in the lossless limit, which are detected by seeking peaks of its derivative, $d\mathrm{Arg}(m_{11})/dk_{//}$, per frequency and wavenumber [Fig. 7(c)]. As a result, we obtain pairs of (ω, $k_{//}$) that correspond to eigenmodes. We note that, in the presence of loss, the peaks of $d\mathrm{Arg}(m_{11})/dk_{//}$ broaden both in ω and $k_{//}$. For more details regarding the RPM, see [41]. This approach can be generalized to account for anisotropic materials by replacing the traditional 2×2 transfer matrix [66] with a 4×4 formalism (see, for example, [67–69]).

Not all eigenmodes of a heterostructure constitute surface waves. For a wave (or mode) to be surface-confined, it is required to be in the optical band gap of both bounding media [70]. In the general case of Fig. 7(a), these are air and the arbitrary layered heterostructure. A surface-confined wave requires an out-of-plane wavenumber k_z that has a nonzero imaginary part, ensuring decay away from the interface $z = 0$. However, for more than one layer, the parameter k_z is not a well-defined quantity. For an A-B-A-$\cdots$ binary photonic crystal, wave propagation in the z direction is usually expressed in terms of the Bloch wavenumber

$$\cos(k_{\mathrm{Bloch}}\Lambda_{\mathrm{char}}) = \frac{m_{11} + m_{22}}{2}, \tag{A1}$$

where Λ_{char} is the period of the photonic crystal and m_{11}, m_{22} are the transfer matrix $\bar{M}$ diagonal elements. The condition for a photonic band is then given by [66]

$$|\cos(k_{\mathrm{Bloch}}\Lambda_{\mathrm{char}})| \leqslant 1. \tag{A2}$$

A mode belonging in a band is allowed to propagate sinusoidally into the structure, with $\mathrm{Re}(k_{\mathrm{Bloch}}) \gg \mathrm{Im}(k_{\mathrm{Bloch}})$. We refer to these modes as photonic or leaky modes in contrast to surface-confined modes that mainly reside at the interface between air and the heterostructure, and decay in the lateral direction.

The condition in Eq. (A1) is limited to infinite and purely periodic binary systems. Here, we generalize this condition to any random finite arrangement, for example, aperiodic, chirped, noncentrosymmetric layered structures, and finite number of layers. Our approach originates from, but is not limited to, metamaterials' homogenization.

Most homogenization schemes are based on S-parameter retrieval approaches [43,71–73], based on which, an arbitrary composite system of finite thickness d and known scattering properties t and r is represented by an effective impedance and an effective out-of-plane wavenumber, Z_{eff} and k_{eff}, respectively. These functions are analytical expressions of the transmission and reflection coefficients. The expression for the effective wavenumber k_{eff} at oblique incidence was derived by Menzel *et al.* [72]:

$$\cos(k_{\mathrm{eff}}d) = \frac{k_s(1-r^2) + k_c(t/A)^2}{(t/A)[k_s(1-r) + k_c(1+r)]}. \tag{A3}$$

For TE polarization, $A = 1$, $k_{\mathrm{c}} = k_{\mathrm{z,c}}$, and $k_{\mathrm{s}} = k_{\mathrm{z,s}}$, whereas for TM polarization $A = \sqrt{\epsilon_{\mathrm{s}}/\epsilon_{\mathrm{c}}}$, $k_c = k_{\mathrm{z,c}}/\epsilon_{\mathrm{c}}$, and $k_{\mathrm{s}} = \mathrm{z, s}/\epsilon_{\mathrm{s}}$, where the subscripts c and s represent the cladding and substrate, with permittivities ϵ_{c} and ϵ_{s}, respectively. Typically, based on the subwavelength thickness of the layers, the parameters Z_{eff} and k_{eff} are translated to constitutive effective parameters, namely, permittivity and permeability, through $k_{\mathrm{eff}} = \sqrt{\epsilon_{\mathrm{eff}}\mu_{\mathrm{eff}}}\frac{\omega}{c}$ and $Z_{\mathrm{eff}} = \sqrt{\frac{\mu_{\mathrm{eff}}}{\epsilon_{\mathrm{eff}}}}$. The conditions under which the assignment of effective parameters ϵ_{eff} and

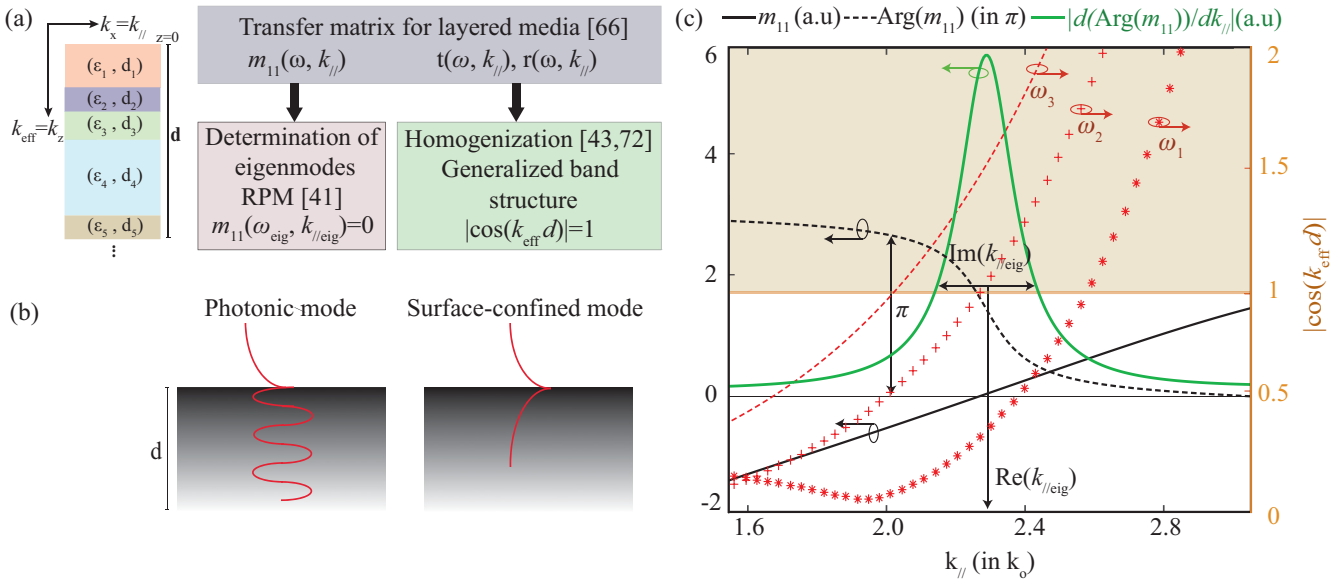

FIG. 7. Surface waves computations. (a) Schematic of an arbitrary layered system (left) and flow chart of the method (right). (b) Definition of a photonic or leaky mode (left) and a surface-confined mode (right), for which $|\cos(k_{\rm eff}(\omega, k_{//})d)| \leqslant 1$ and $|\cos(k_{\rm eff}(\omega, k_{//})d)| > 1$, respectively. (c) Combination of RPM [41] with our generalized band structure condition [Eq. (A4)] for the distinction between photonic (leaky) and surface-confined eigenmodes: At the eigenmode's in-plane wavenumber $k_{//\rm eig}$, m_{11} vanishes (black solid curve), $\mathrm{Arg}(m_{11})$ drops by π (black dashed curve), and its derivative $d\mathrm{Arg}(m_{11})/dk_{//}$ resonates (green curve). The highlighted region corresponds to a band gap ($|\cos(k_{\rm eff}d)| > 1$). For frequency ω_1, the mode is photonic, as it resides inside the band, whereas for ω_2 the mode is located at the band edge. For ω_3, the mode is surface confined, propagating at the air-heterostructure interface.

$\mu_{\rm eff}$ is valid are complex [74,75] and remain an area of active literature discussion [25,76].

By contrast, the description of a system in terms of an effective impedance and a wavenumber, $Z_{\rm eff}$ and $k_{\rm eff}$, respectively, remains valid at any scale. Since $k_{\rm eff}$ is directly associated with the scattering coefficients t and r [Eq. (A3)] [71–73], it can be used for describing an arbitrary heterostructure at any scale, not necessarily in the metamaterial subwavelength limit, as long as t and r may be computed. As a sanity check, it is straightforward to notice that the Bloch wavenumber $k_{\rm Bloch}$ in Eq. (A1) is a special case of $k_{\rm eff}$ in Eq. (A3) for binary, purely periodic systems, when the cladding and substrate are composed of the same material ($\epsilon_s = \epsilon_c$). This may be seen by expressing t and r in Eq. (A3) in terms of transfer matrix elements, using the identity $\det(\bar{M}) = 1$, and the fact that $m_{21} = m_{12}^*$ for purely dielectric materials (where m_{21} and m_{12} are purely imaginary), and $m_{21} = -m_{12}$ for dispersive materials [66].

To summarize, for an excitation to be considered as a surface wave, three conditions must be satisfied: first, it has to be an eigenmode of the structure, which we evaluate with the RPM; second, it has to be in the optical band gap of the surrounding medium ($k_{//} > k_{\rm o}$); and third, it has to be in the band gap of the heterostructure. This third condition is implemented by introducing the notion of a generalized band structure, applicable to *any* planar configuration, based on Eq. (A3) and $k_{\rm eff}$. A band is a set of $(\omega, k_{//})$ for which

$$|\cos(k_{\rm eff}d)| \leqslant 1. \tag{A4}$$

Surface waves exist at the exterior of a band or at its edge ($|\cos(k_{\rm eff}d)| \geqslant 1$).

We demonstrate this methodology: in Fig. 7(c) we study an eigenmode of a planar structure. At the eigenmode's in-plane wavenumber $k_{//\rm eig}$, the matrix element m_{11} vanishes (black curve); therefore, its phase $\mathrm{Arg}(m_{11})$ drops by π (black dashed curve). Taking the derivative of m_{11} with respect to $k_{//}$, we obtain a peak, as shown with the green curve. Its half-width-half-maximum corresponds to the in-plane decay length through $L = 1/2\mathrm{Im}(k_{//\rm eig})$. In order to determine the nature of the mode (photonic or surface-confined), we employ our generalized band edge condition [Eq. (A4)]. The quantity $|\cos(k_{\rm eff}d)|$ is shown for three different frequencies ω_1, ω_2, and ω_3 (right vertical axis). For ω_1, $|\cos(k_{\rm eff}d)| < 1$ at $k_{//\rm eig}$, and this mode belongs to a photonic band, resulting in propagation inside the heterostructure; in other words, it is a photonic or leaky mode. For ω_2, the parameter $|\cos(k_{\rm eff}d)|$ crosses unity at $k_{//\rm eig}$ and this mode is located exactly at the band edge. Finally, for frequency ω_3, the mode is inside the band gap, highlighted in Fig. 7(c) with the upper orange shaded area, and the mode is forbidden from propagating inside the structure; in other words, it is surface-confined. By retrieving $k_{\rm eff}$, we are also able to estimate the degree of confinement through the penetration depth $t = 1/2\mathrm{Im}(k_{\rm eff})$.

APPENDIX B: OPTICAL PROPERTIES

Here, we append the optical properties for the materials used in this work. For the electric permittivity of silver we used the Drude model [38], with $\omega_{\rm p} = 13.69 \times 10^{15}$ rad/s and $\gamma_{\rm m} = 0.7292 \times 10^{14}$ rad/s from [38]. We modeled SiC, WS_2, MoS_2, WSe_2, and $MoSe_2$ with the Lorentz permittivity

TABLE I. Lorentz parameters [Eq. (2)] for the materials considered in Figs. 4–6. ω_{TO}, ω_{LO}, and γ_d are presented in units of rad/s.

	$\epsilon_{\infty,d}$	ω_{TO}	ω_{LO}	γ_d
SiC	6.7	1.49×10^{14}	1.83×10^{14}	8.97×10^{11}
WS_2	18	2.995×10^{15}	3.021×10^{15}	8.094×10^{13}
MoS_2	20.4	2.754×10^{15}	2.81×10^{15}	1.1×10^{14}
WSe_2	18.3	2.502×10^{15}	2.523×10^{15}	1.4×10^{14}
$MoSe_2$	25.3	2.37×10^{15}	2.395×10^{15}	1.25×10^{14}
WS_2(mono)	17	3.053×10^{15}	3.085×10^{15}	3.94×10^{13}
MoS_2(mono)	21	2.837×10^{15}	2.878×10^{15}	1×10^{14}
WSe_2(mono)	15.3	2.512×10^{15}	2.543×10^{15}	7.813×10^{13}
$MoSe_2$(mono)	21.3	2.355×10^{15}	2.377×10^{15}	8×10^{13}

in Eq. (2). The optical properties for SiC were taken from [11,12,44], while the TMD optical properties were extracted from [15]. In Table I, we present the parameters $\epsilon_{\infty,d}$, ω_{TO}, ω_{LO}, and γ_d for each of these materials. For TMDs, bulk and monolayer parameters are displayed separately.

We note that calculations for TMDs were carried out at different frequency ranges, based on the location of the most prominent exciton permittivity resonance in each material. Calculations were centered around ω_{TO}, while spanning the frequency range displayed on the vertical axes in Figs. 5 and 6. The quality factors for the considered materials are $Q_{SiC} = 166$, $Q_{MoSe_2} = 19$, $Q_{WSe_2} = 18$, $Q_{MoS_2} = 25$, and $Q_{WS_2} = 37$, $Q_{MoSe_2,mono} = 29$, $Q_{WSe_2,mono} = 32$, $Q_{MoS_2,mono} = 26$, and $Q_{WS_2,mono} = 77$.

[1] J. N. Anker, W. P. Hall, O. Lyandres, N. C. Shah, J. Zhao, and R. P. Van Duyne, Nat. Mater. **7**, 442 (2008).
[2] M. Xiao, R. Jiang, F. Wang, C. Fang, J. Wang, and J. C. Yu, J. Mater. Chem. A **1**, 5790 (2013).
[3] D. J. Bergman and M. I. Stockman, Phys. Rev. Lett. **90**, 027402 (2003).
[4] P. Berini and I. De Leon, Nat. Photon. **6**, 16 (2012).
[5] M. A. Noginov, G. Zhu, M. Mayy, B. A. Ritzo, N. Noginova, and V. A. Podolskiy, Phys. Rev. Lett. **101**, 226806 (2008).
[6] S. P. Burgos, H. W. Lee, E. Feigenbaum, R. M. Briggs, and H. A. Atwater, Nano Lett. **14**, 3284 (2014).
[7] D. Kalavrouziotis, S. Papaioannou, K. Vyrsokinos, A. Kumar, S. Bozhevolnyi, L. Markey, J.-C. Weeber, A. Dereux, G. Giannoulis, D. Apostolopoulos, H. Avramopoulos, and N. Pleros, in *Optical Fiber Communication Conference* (Optical Society of America, Bellingham, WA, 2012), p. OW3E.3.
[8] H. W. Lee, G. Papadakis, S. P. Burgos, K. Chander, A. Kriesch, R. Pala, U. Peschel, and H. A. Atwater, Nano Lett. **14**, 6463 (2014).
[9] T. Nakamura, Phys. Rev. Appl. **6**, 044009 (2016).
[10] A. Tcherniak, S. Dominguez-Medina, W.-S. Chang, P. Swanglap, L. S. Slaughter, C. F. Landes, and S. Link, J. Phys. Chem. C **115**, 15938 (2011).
[11] H. Iizuka and S. Fan, Phys. Rev. Lett. **120**, 063901 (2018).
[12] K. Joulain, J.-P. Mulet, F. Marquier, R. Carminati, and J.-J. Greffet, Surf. Sci. Rep. **57**, 59 (2005).
[13] E. N. Economou, Phys. Rev. **182**, 539 (1969).
[14] J. Caldwell, L. Lindsay, V. Giannini, I. Vurgaftman, T. Reinecke, S. Maier, and O. Glembocki, Nanophotonics **4**, 44 (2015).
[15] Y. Li, A. Chernikov, X. Zhang, A. Rigosi, H. M. Hill, A. M. van der Zande, D. A. Chenet, E.-M. Shih, J. Hone, and T. F. Heinz, Phys. Rev. B **90**, 205422 (2014).
[16] A. Polman and H. A. Atwater, Mater. Today **8**, 56 (2005).
[17] A. Woessner, M. B. Lundeberg, Y. Gao, A. Principi, P. Alonso-González, M. Carrega, K. Watanabe, T. Taniguchi, G. Vignale, M. Polini, J. Hone, R. Hillenbrand, and F. H. L. Koppens, Nat. Mater. **14**, 421 (2015).
[18] Z. Jacob, J.-Y. Kim, G. V. Naik, A. Boltasseva, E. E. Narimanov, and V. M. Shalaev, Appl. Phys. B **100**, 215 (2010).
[19] L. Landau, E. Lifshitz, and L. P. Pitaevskii, in *Electrodynamics of Continuous Media*, Course of Theoretical Physics (Pergamon Press, New York, 1984), Vol. 8, p. 2.
[20] P. Li, M. Lewin, A. V. Kretinin, J. D. Caldwell, K. S. Novoselov, T. Taniguchi, K. Watanabe, F. Gaussmann, and T. Taubner, Nat. Commun. **6**, 7507 (2015).
[21] J. D. Caldwell, O. J. Glembocki, Y. Francescato, N. Sharac, V. Giannini, F. J. Bezares, J. P. Long, J. C. Owrutsky, I. Vurgaftman, J. G. Tischler, V. D. Wheeler, N. D. Bassim, L. M. Shirey, R. Kasica, and S. A. Maier, Nano Lett. **13**, 3690 (2013).
[22] V. E. Ferry, M. A. Verschuuren, H. B. T. Li, E. Verhagen, R. J. Walters, R. E. I. Schropp, H. A. Atwater, and A. Polman, Opt. Exp. **18**, A237 (2010).
[23] H. A. Atwater and A. Polman, Nat. Mater. **9**, 205 (2010).
[24] G. T. Papadakis, D. Fleischman, A. Davoyan, P. Yeh, and H. A. Atwater, Nat. Commun. **9**, 296 (2018).
[25] R. Merlin, Proc. Natl. Acad. Sci. USA **106**, 1693 (2009).
[26] R. Alexander and R. Bell, Opt. Commun. **10**, 59 (1974).
[27] N. Sang-Nourpour, B. R. Lavoie, R. Kheradmand, M. Rezaei, and B. C. Sanders, J. Opt. **19**, 125004 (2017).
[28] M. Kawachi, Opt. Quantum Electron. **22**, 391 (1990).
[29] P. Dong, W. Qian, S. Liao, H. Liang, C.-C. Kung, N.-N. Feng, R. Shafiiha, J. Fong, D. Feng, A. V. Krishnamoorthy, and M. Asghari, Opt. Exp. **18**, 14474 (2010).
[30] P. K. Tien and R. Ulrich, J. Opt. Soc. Am. **60**, 1325 (1970).
[31] P. K. Tien, Appl. Opt. **10**, 2395 (1971).
[32] P. K. Cheo, Appl. Phys. **6**, 1 (1975).
[33] S. W. Koch, M. Kira, G. Khitrova, and H. M. Gibbs, Nat. Mater **5**, 523 (2006).
[34] R. Hillenbrand, T. Taubner, and F. Keilmann, Nature (London) **418**, 159 (2002).
[35] S. Amarie and F. Keilmann, Phys. Rev. B **83**, 045404 (2011).
[36] J. B. Khurgin, Optica **2**, 740 (2015).
[37] X. Liu, W. Bao, Q. Li, C. Ropp, Y. Wang, and X. Zhang, Phys. Rev. Lett. **119**, 027403 (2017).
[38] A. D. Rakić, A. B. Djurišić, J. M. Elazar, and M. L. Majewski, Appl. Opt. **37**, 5271 (1998).
[39] J. A. Dionne, L. A. Sweatlock, H. A. Atwater, and A. Polman, Phys. Rev. B **73**, 035407 (2006).
[40] A. R. Davoyan and N. Engheta, ACS Photon. **3**, 737 (2016).
[41] E. Anemogiannis, E. N. Glytsis, and T. K. Gaylord, J. Lightwave Technol. **17**, 929 (1999).
[42] Y. t. Fang, L. k. Chen, N. Zhu, and J. Zhou, IET Optoelect. **7**, 9 (2013).
[43] G. T. Papadakis, P. Yeh, and H. A. Atwater, Phys. Rev. B **91**, 155406 (2015).

[44] W. G. Spitzer, D. Kleinman, and D. Walsh, Phys. Rev. **113**, 127 (1959).
[45] D. F. Edwards and E. Ochoa, Appl. Opt. **19**, 4130 (1980).
[46] D. E. Aspnes and A. A. Studna, Phys. Rev. B **27**, 985 (1983).
[47] S. Dai, Z. Fei, Q. Ma, A. S. Rodin, M. Wagner, A. S. McLeod, M. K. Liu, W. Gannett, W. Regan, K. Watanabe, T. Taniguchi, M. Thiemens, G. Dominguez, A. H. C. Neto, A. Zettl, F. Keilmann, P. Jarillo-Herrero, M. M. Fogler, and D. N. Basov, Science **343**, 1125 (2014).
[48] D. N. Basov, M. M. Fogler, and F. J. García de Abajo, Science **354**, aag1992 (2016).
[49] Z. Fei, M. E. Scott, D. J. Gosztola, J. J. Foley, J. Yan, D. G. Mandrus, H. Wen, P. Zhou, D. W. Zhang, Y. Sun, J. R. Guest, S. K. Gray, W. Bao, G. P. Wiederrecht, and X. Xu, Phys. Rev. B **94**, 081402 (2016).
[50] C. Manolatou, H. Wang, W. Chan, S. Tiwari, and F. Rana, Phys. Rev. B **93**, 155422 (2016).
[51] V. D. Karanikolas and E. Paspalakis, Phys. Rev. B **96**, 041404 (2017).
[52] H. J. Lezec, J. A. Dionne, and H. A. Atwater, Science **316**, 430 (2007).
[53] S. A. Maiera and H. A. Atwater, J. Appl. Phys. **98**, 011101 (2005).
[54] M. V. Bashevoy, F. Jonsson, A. V. Krasavin, N. I. Zheludev, Y. Chen, and M. I. Stockman, Nano Lett. **6**, 1113 (2006).
[55] D. Fleischman, L. A. Sweatlock, H. Murakami, and H. Atwater, Opt. Exp. **25**, 27386 (2017).
[56] J. A. Dionne, E. Verhagen, A. Polman, and H. A. Atwater, Opt. Exp. **16**, 19001 (2008).
[57] C. Chen, P. Berini, D. Feng, S. Tanev, and V. P. Tzolov, Opt. Exp. **7**, 260 (2000).
[58] R. Rodriguez-Berral, F. Mesa, and F. Medina, IEEE Trans. Microwave Theory Technol. **53**, 1613 (2005).
[59] J. Zhu, X. Zhang, and R. Song, J. Lightwave Technol. **28**, 1802 (2010).
[60] W.-J. Hsueh and J.-C. Lin, J. Opt. Soc. Am. A **24**, 825 (2007).
[61] L. A. Sweatlock and K. Diest, Opt. Exp. **20**, 8700 (2012).
[62] A. Khalatpour, J. Mu, K. Moussakhani, and W. P. Huang, J. Lightwave Technol. **28**, 2851 (2010).
[63] Y. Zhou, X. Yu, Y. Zhang, H. Zhang, and H.-P. Ho, in *Proceedings of the 2010 Photonics Global Conference* (IEEE, New York, 2010), pp. 1–5.
[64] J. Petracek and K. Singh, IEEE Photon. Technol. Lett. **14**, 810 (2002).
[65] A. Hosseini, A. Nieuwoudt, and Y. Massoud, Opt. Exp. **14**, 7291 (2006).
[66] P. Yeh, *Optical Waves in Layered Media*, 2nd ed., Wiley Series in Pure and Applied Optics (Wiley-Interscience, New York, 2005).
[67] N. C. Passler and A. Paarmann, J. Opt. Soc. Am. B **34**, 2128 (2017).
[68] P. Yeh, J. Opt. Soc. Am. **69**, 742 (1979).
[69] D. W. Berreman, J. Opt. Soc. Am. **62**, 502 (1972).
[70] M. Xiao, Z. Q. Zhang, and C. T. Chan, Phys. Rev. X **4**, 021017 (2014).
[71] D. R. Smith, D. C. Vier, T. Koschny, and C. M. Soukoulis, Phys. Rev. E **71**, 036617 (2005).
[72] C. Menzel, C. Rockstuhl, T. Paul, F. Lederer, and T. Pertsch, Phys. Rev. B **77**, 195328 (2008).
[73] X. Chen, T. M. Grzegorczyk, B.-I. Wu, J. Pacheco, and J. A. Kong, Phys. Rev. E **70**, 016608 (2004).
[74] A. Alù, Phys. Rev. B **83**, 081102 (2011).
[75] A. Alù and N. Engheta, Phys. Rev. B **78**, 085112 (2008).
[76] T. Koschny, P. Markoš, D. R. Smith, and C. M. Soukoulis, Phys. Rev. E **68**, 065602 (2003).